Dip coating of air purifier ceramic honeycombs with photocatalytic TiO$_2$ nanoparticles: A case study for occupational exposure

Antti Joonas Koivisto [a,*], Kirsten Inga Kling [a], Ana Sofia Fonseca [a], Anders Brostrøm Bluhme [a,b], Marcel Moreman [c], Mingzhou Yu [d,e], Anna Luisa Costa [f], Baldi Giovanni [g], Simona Ortelli [f], Wouter Fransman [c], Ulla Vogel [a], Keld Alstrup Jensen [a]

[a] National Research Centre for the Working Environment, Lersø Parkallé 105, Copenhagen DK-2100, Denmark
[b] Technical University of Denmark, Department of Micro- and Nanotechnology, Ørsteds Plads, Building 345B, DK-2800 Kgs. Lyngby, Denmark
[c] TNO, PO Box 360, 3700AJ Zeist, The Netherlands
[d] China Jiliang University, Hangzhou, China
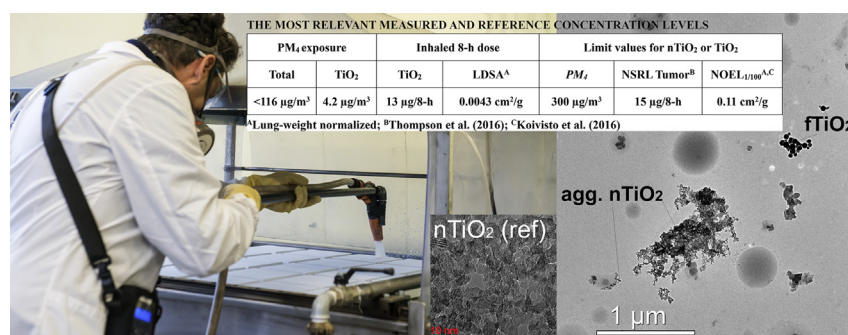[e] Key Laboratory of Aerosol Chemistry and Physics, Chinese Academy of Science, Xi'an, China
[f] CNR-ISTEC, Via Granarolo, 64, 48018 Faenza, RA, Italy
[g] COLOROBBIA CONSULTING S.r.L., Via Pietramarina 53, 50053, Sovigliana, Vinci, FI, Italy

HIGHLIGHTS

- Workers exposure to TiO$_2$ was assessed during application of photoactive coating.
- Fine- and nano-TiO$_2$ released by air blade drying and no release by dip coating
- Emission rates: 420×10^9 min^{-1}, 1.33×10^9 µm^2 min^{-1}, and 3.5 mg min^{-1} (~3.7% TiO$_2$)
- TiO$_2$ exposure was 4.2 µg m^{-3}; 8-h calculated doses were 4.3×10^{-3} cm^2 g^{-1} and 13 µg.
- Nano-TiO$_2$ was found as agglomerates and coagulated with background particles.

GRAPHICAL ABSTRACT

ABSTRACT

Nanoscale TiO$_2$ (nTiO$_2$) is manufactured in high volumes and is of potential concern in occupational health. Here, we measured workers exposure levels while ceramic honeycombs were dip coated with liquid photoactive nanoparticle suspension and dried with an air blade. The measured nTiO$_2$ concentration levels were used to assess process specific emission rates using a convolution theorem and to calculate inhalation dose rates of deposited nTiO$_2$ particles. Dip coating did not result in detectable release of particles but air blade drying released fine-sized TiO$_2$ and nTiO$_2$ particles. nTiO$_2$ was found in pure nTiO$_2$ agglomerates and as individual particles deposited onto background particles. Total particle emission rates were 420×10^9 min^{-1}, 1.33×10^9 µm^2 min^{-1}, and 3.5 mg min^{-1} respirable mass. During a continued repeated process, the average exposure level was 2.5×10^4 cm^{-3}, 30.3 µm^2 cm^{-3}, <116 µg m^{-3} for particulate matter. The TiO$_2$ average exposure level was 4.2 µg m^{-3}, which is well below the maximum recommended exposure limit of 300 µg m^{-3} for nTiO$_2$ proposed by the US National Institute for Occupational Safety and Health. During an 8-hour exposure, the observed concentrations would result in a lung deposited surface area of 4.3×10^{-3} cm^2 g^{-1} of lung tissue and 13 µg of TiO$_2$ to the trachea-bronchi, and alveolar regions. The dose levels were

* Corresponding author.
  E-mail address: jok@nrcwe.dk (A.J. Koivisto).

well below the one hundredth of the no observed effect level ($NOEL_{1/100}$) of 0.11 $cm^2\ g^{-1}$ for granular biodurable particles and a daily no significant risk dose level of 44 μg day^{-1}. These emission rates can be used in a mass flow model to predict the impact of process emissions on personal and environmental exposure levels.

1. Introduction

The photocatalytic properties of nanoscale titanium dioxide ($nTiO_2$), especially in its anatase form, are superior as compared to other photocatalysts such as ZnO, ZrO_2, SnO_2, WO_3, CeO_2, ZnS, and Fe_2O_3 (Mo et al., 2009). This makes $nTiO_2$ one of the most used nanomaterials globally (Piccinno et al., 2012; Robichaud et al., 2009; Ramos-Delgado et al., 2016). One of the main applications of $nTiO_2$ is in photocatalytic degradation of organic contaminants in the air (Mo et al., 2009; Yu and Kim, 2013; Mamaghani et al., 2017; Ren et al., 2017; Zhong and Haghighat, 2015; Chen et al., 2015; Ortelli et al., 2016) and aqueous environments (Szczepanik, 2017; Garcia-Segura and Brillas, 2017). Currently, there is a high interest in photocatalytic air purification applications for both indoor and outdoor use (Zhong and Haghighat, 2015) because air pollution is recognized globally as one of the major risk factors for human health (Health Effects Institute, 2017; European Environmental Agency, 2017).

A number of studies of different exposure scenarios have shown that it is possible for workers to be exposed to $nTiO_2$ in a number of work situations. During liquid flame spray synthesis, the exposure levels were *ca.* $2 \times 10^3\ cm^{-3}$, when the spray gun was located in a fully closed glove box (Demou et al., 2009), $10^5\ cm^{-3}$ in a ventilated chamber (Koivisto et al., 2012a), and $>10^7\ cm^{-3}$ during coating of substrates under a hood (Koivisto et al., 2012a, 2015). Particles were below 200 nm in size, hence mass concentrations were low (*e.g.* 1.7 μg m^{-3} during synthesis in a ventilated chamber; Koivisto et al., 2012a). In contrast, Fonseca et al. (2018) did not detect any increase in particle concentrations during sol-gel-synthesis of $nTiO_2$ by thermal decomposition of $TiCl_4$ inside a fume hood.

Koivisto et al. (2012b) measured during industrial jet milling and packing of $nTiO_2$ PM_{10} mass concentration level of *ca.* 100 μg m^{-3} and during dumping of $nTiO_2$ bags, peak concentrations reached momentarily up to 3 mg m^{-3}. Xu et al. (2016) measured 0.79 and 3.17 mg m^{-3} PM_{10} mass concentrations in a milling and packing workshop, respectively, but further analysis showed that TiO_2 PM_{10} mass concentration was 39.4 and 46.4 μg $TiO^2\ m^{-3}$, respectively. Kaminski et al. (2015) measured up to 0.55 mg m^{-3} PM_{10} mass concentrations in different $nTiO_2$ packing areas and up to 19 μg m^{-3} in production area. In a small scale industrial $nTiO_2$ production of 5 kg h^{-1}, Lee et al. (2011) measured during $nTiO_2$ synthesis and powder collection mass concentration levels of 0.10 to 4.99 mg m^{-3}. Spinazzè et al. (2016) measured workers exposure levels during application of photoactive $nTiO_2$ suspension onto concrete blocks with an automatic electrostatic spraying system, but the coating process did not increase the concentration levels as compared to background levels or other parts of the facility.

Emission rates can be used to predict exposure levels and mass flows in different environments (*e.g.* Hewett and Ganser, 2017; Ganser and Hewett, 2017). Koivisto et al. (2017) showed that composites containing $nTiO_2$ from 0.7 to 10 weight % (wt%) released airborne particles at emission rates from *ca.* 600 to $6 \times 10^{10}\ min^{-1}$ during wind erosion exposure, abrasion, and sanding. The released particles were mainly matrix fragments with $nTiO_2$ particles embedded. The application of photocatalytic $nTiO_2$ coating with pump spray released *ca.* 2×10^8 particles per applied g of the product (Koivisto et al., 2017). A particle number emission rate of $1.1 \times 10^{12}\ min^{-1}$ and a mass emission rate of 23 mg min^{-1} were observed during electrostatic spray deposition of a photoactive suspension containing 0.2 wt% $nTiO_2$ particles for particles in the size range of 5.5 nm to 30 μm (Koivisto et al., 2018).

In general, emission rates are usually given in particle number but not in surface area or mass units, which make exposure and risk assessment challenging (Koivisto et al., 2017). For TiO_2, biological effects are usually studied as a function of administrated surface area or mass dose (Schmid and Stoeger, 2016; Thompson et al., 2016; Mihalache et al., 2017). Currently, the pigment grade TiO_2 occupational exposure limits (OELs) vary from 4 to 10 mg m^{-3} and the recommended exposure limit (REL) values assigned for $nTiO_2$ range from 17 to 2000 μg m^{-3}, depending on the parameterization of the risk assessment model (Mihalache et al., 2017).

Dip coating is the most popular technique to apply photoactive coatings to substrates in laboratory scale productions (Puddu et al., 2010). Here, we assessed workers' exposure to airborne particles during dip coating of ceramic honeycomb cells (HCs) with a photoactive $nTiO_2$ suspension and during drying of the coated HCs with an air blade, respectively. We measured particle concentrations in the Near Field (NF), Far Field (FF), breathing zone (BZ), and in an adjacent laboratory room and a hall. The concentrations were used to calculate process specific particle emission rates in particle number, surface area, and mass. The workers' inhalation dose rates of deposited particles were calculated from the measured particle number size distributions and lung deposited surface area concentrations. Results from structural and chemical characterisation of particles by electron microscopy were used to discriminate particles from different sources. The exposure levels and regional deposited doses of TiO_2 during inhalation were used to estimate the inhalation exposure risk of process particle emissions.

2. Materials and methods

2.1. Coating product

The photoactive suspension (PARNASOS® PH000025, COLOROBBIA CONSULTING S.r.l., Vinci, Italia) consisted of acidic water with pH 1.0 ± 0.5 containing 1–5 wt% Propan-2-ol (CAS: 67-63-0), 1–5 wt% hydrochloric acid (CAS: 7647-01-0), and 6.0 ± 0.5 wt% anatase $nTiO_2$ particles (CAS: 13463-67-7). The $nTiO_2$ particles (Fig. A.1, Supplementary material) were synthesized by the acid hydrolysis in sol-gel process (details N/A) and the average particle size in the suspension was 40 ± 10 nm (ZetaSizer ZS DLS, Malvern Instruments Ltd, Worcestershire, United Kingdom). The photoactive suspension PARNASOS® PH000025 can be applied on different substrates by dip coating. The material data sheet is given in Appendix B, Supplementary material, and the material safety data sheet in Appendix C, Supplementary material.

2.2. Work environment and the coating process

The coating was performed in a ventilated chamber located at an industrial research laboratory at Colorobbia S.p.A, Florence, Italy (Fig. 1). The coating room (V = 390.4 m^3) was ventilated by natural air exchange (λ_n; air flow rate N/A) and by two local exhaust ventilations (LEV_C and LEV_R; Fig. 1). LEV_C (chamber) was on during the dip coating process and LEV_R (room) was continuously on. Ventilation replacement air was taken without filtration from outdoors and from an adjacent laboratory room and a hall at unknown flow rates.

The entire process cycle consisted of three phases: 1) dip coating of 25 untreated HCs ($15 \times 15 \times 2\ cm^3$ each) placed in a grit holder for 10 ± 1 min; 2) air blade drying the HCs for 50 ± 10 s; and 3) removing the coated HCs from and cleaning of the chamber grit holder with air blade for 5 ± 2 s. The process cycle including pauses between different
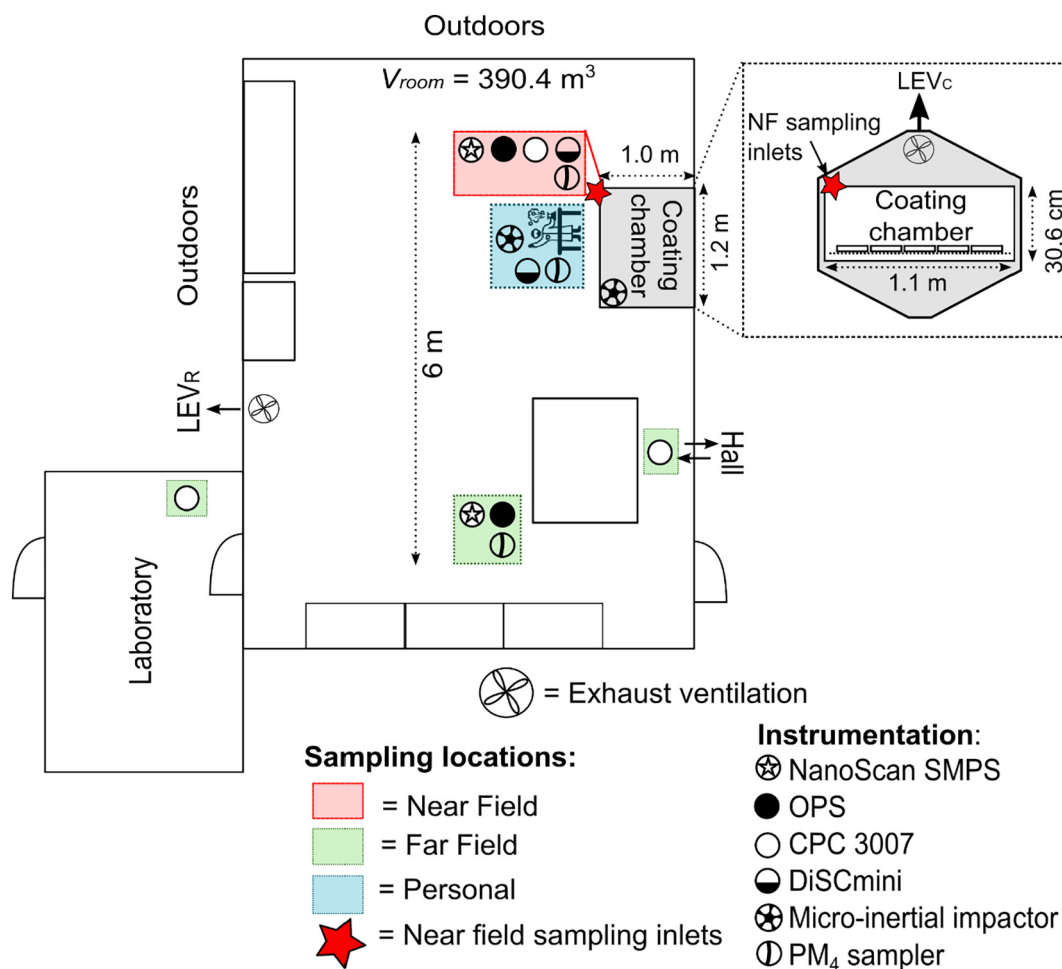
Fig. 1. Layout of the process area and instrumentation.

process phases was 20 min, resulting in a coating rate of 25 HCs 20 min^{-1}. The suspension was applied to the HCs with a garden hose nozzle at a flow rate of 36 L min^{-1} and collected from the bottom of the chamber and recirculated using a pump. The process cycle was repeated 4 times.

During dip coating and air blade cleaning a worker was within a 50 cm range from the chamber opening. Another worker stored coated HCs and passed uncoated HCs for coating within 5 m from the chamber. The workers wore filtering face piece respirators (CE certified to EN 14387:2004), laboratory eyeglasses, cotton clothing and nitrile gloves.

Flow rates of LEV$_C$ and LEV$_R$ were measured using a vane probe (435-2, Testo, Lenzkirch, Germany, measurement range 0.6–40 m s^{-1}) and a hot-wire anemometer (435-2, Testo, Lenzkirch, Germany, measurement range 0.03–20 m s^{-1}).

The relative humidity and temperature in the work-room was recorded by Gemini TinytagPlus Data Loggers (Gemini Data Loggers Ltd, West Sussex, UK).

The LEV$_C$ and LEV$_R$ volume flow rates were 7.44 and 2.2 m^3 min^{-1}, respectively, when assuming uniform flow in the ventilation duct. Between 11:00 and 19:00, the room temperature and relative humidity were 21.6 ± 1.2 °C and 38 ± 3%, respectively.

2.3. Particle measurements and sampling

Particle number concentrations, size-distributions, lung-deposited surfaces areas (LDSA) and respirable dust mass-concentrations were measured from NF and FF locations (Fig. 1) at heights from 1.0 to 1.3 m while personal exposure measurements of respirable dust and LDSA was made from within 30 cm of workers personal breathing zone (BZ). The real-time particle measurements included:

- Particle mobility size distributions measured by NanoScans (NanoScan; TSI NanoScan model 3091, TSI Inc., Shoreview, MN, USA) for particles from 10 to 420 nm in 60 s intervals.
- Particle optical size distributions measured by optical particle sizers (OPS; TSI model 3330, TSI Inc., Shoreview, MN, USA) for particles from 300 nm to 10 μm in 60 s intervals.
- Particle LDSA concentrations (μm^2 cm^{-3}) measured with diffusion chargers (DC; DiSCmini; 0.7 μm pre-impactor; Matter Aerosol AG, Wohlen, Switzerland) for particles from 10 to 700 nm in 1 s intervals.
- Particle number concentrations measured by condensation particle counters (CPC; TSI model 3007, TSI Inc., Shoreview, MN, USA) from 10 nm to >1 μm in 1 s intervals.

Worker BZ LDSA concentration was measured by using a DC and respirable dust ($PM_{4,BZ}$) was collected on 37 mm PTFE filters with a 0.8 μm pore size (Millipore, Billerica, MA, USA) mounted in sampling cyclones BGI Model GK2.69 (Q_s = 4.2 L min^{-1}; BGI Inc., Waltham, MA, USA). FF respirable dust ($PM_{4,FF}$) was collected on 37 mm PFTE filters with a 0.8 μm pore size (Millipore, Billerica, MA, USA) by using BGI Model SCC 1.062 cyclones (Q_s = 1.05 L min^{-1}). The filters were used for both gravimetric and X-ray fluorescence (XRF) analysis.

Filter- weighing was made in a climate controlled room at 50 ± 5% relative humidity and constant temperature of 22 ± 1 °C after >24 h of acclimatization. The weight of each filter was corrected for handling

and environmental factors by using three blind filters. After weighing, the sampled filters were stored in the climate controlled room for subsequent chemical characterisation.

Airborne particles were collected inside the coating chamber and in the worker breathing zone at 15:11 for 60 s by using a micro-inertial impactor (Kandler et al., 2007) on carbon coated Ni-TEM grids (Plano, Wetzlar, Germany). The sample was collected onto three impaction stages at flow rate of 0.48 L min^{-1}, which results in calculated d_{50} cutoff diameters of 1.3, 0.5, and 0.05 μm.

2.4. Physico-chemical particle characterisation

Particles collected on TEM Grids were analyzed using a Transmission Electron Microscopy (TEM; Tecnai G20 T2, FEI, Eindhoven, The Netherlands) and a Scanning Electron Microscopy (SEM; Nova NanoSEM 600, FEI, Eindhoven, The Netherlands) coupled with an Energy Dispersive X-ray spectroscopy detector (SEM/EDS; Quantax EDS and Optimus TKD, Bruker, Berlin, Germany). TEM images were recorded at 5000–285000× magnifications to achieve an overview as well as structural information for particle characterisation. SEM secondary electron (SE) and scanning transmission electron microscopy (STEM) images were recorded in an automated manner at 10,000× magnifications. Particles were detected by their grey scale contrast in SE images and EDS spectra's were recorded for the detected area of each individual particle respectively, alongside with size and morphology information.

From the EDS, a Ti Index was calculated in wt% considering all elements detected. This displays the ratio of Ti to all other elements in each individual particle. The Ti index was used to assess the Ti content in the particle phase at different size fractions. This approach has been used describe particle chemical properties of environmental (Lieke et al., 2011; Kandler et al., 2011), occupational (Kling et al., 2016), and combustion particles (Lieke et al., 2013).

The bulk chemical elemental composition of the respirable dust was determined by wave-length dispersive spectrometry XRF using a Bruker Tiger S8 (Bruker, Karlsruhe, Germany). For calibration and determination of the Ti content of the samples, a method applying internal standards was used. The method ("best detection" in QuantExpress, SpecPlus V.3, Bruker, Karlsruhe, Germany) is setup for quantification of multiple elements calibrated with a set of glass standards of known composition and scans over a range of settings in order to detect and quantify amounts of the considered element in ppm.

2.5. Treatment of particle monitoring data and mass unit conversion

The particle size distributions measured by the NanoScan and OPS were combined to one $dN/dLog(D_p)$ particle number size distribution for both NF and FF measurements. Here, the NanoScan last size channel (no. 15) was removed and the 14th channel was cut so that the upper boundary limit was the same as the OPS 1st size channel lower boundary limit (here 300 nm). Then, we calculated a new geometric mean diameter D_p and channel width $dLog(D_p)$ values for the cut channel. The combined particle size distribution, named according to the measurement location as N_{NF} or N_{FF}, was based on the mobility size concentrations from 10 to 300 nm and optical size concentrations from 300 nm to 10 μm. Because the overlap in particle size distributions measured by the NanoScan and OPS is only 120 nm we could not assess the real part of the equivalent refractive index of airborne particles (Vratolis et al., 2018). Thus, we assume that mobility and optical particle diameters are the same when using the OPS default refractive index of 1.59 + 0i. The sampling diffusion losses of the NF NanoScan were corrected according to Cheng (2001).

The NF particle number size distribution was converted to mass size distribution by assuming that particles are spherical and the particle density do not vary with particle size. The density of agglomerates is expected to decrease as the particle size increases (e.g. Rissler et al., 2014). In this case, we do not know the relation between particle size and the

density, thus the density was assumed to be constant. The particle density was set so that the $PM_{4,BZ}$ and the NF respirable mass concentration averaged over the gravimetric sampler respective sampling period were the same. The mass size distribution covering the particle size range of 10 nm to 10 μm ($m_{<10μm}$) was converted to respirable mass size distribution (m_{PM4}) by using the simplified respirable fraction penetration efficiency according to Hinds (1999). It is assumed that the NF and BZ particles are the same in composition and the aerodynamic diameter and the optical diameter are the same.

2.6. Inhalation dose rate calculation

The deposition rate of particles during inhalation was calculated by multiplying particle size concentrations with, the simplified ICRP (1994) human respiratory tract model deposition probability for the upper airways, the tracheobronchial region, and the alveolar region (Hinds, 1999) and a respiratory minute volume of 25 L min^{-1}, which corresponds to the typical respiration rate of a 70 kg male during light exercise. In this calculation, we assumed that particle aerodynamic diameters are the same as measured optical and mobility diameters, i.e. bulk density and effective density are the same (Rostedt et al., 2009), and that hygroscopic growth of particles in the airways is insignificant.

The LDSA dose (cm^{-2}) was calculated from the measured LDSA concentration (μm^2 cm^{-3}). The daily pulmonary deposited particle dose was estimated and considering for an 8-hour workday and the assumptions above resulting in a total inhaled volume of 12 m^3.

2.7. Particle dynamics

Assuming that concentrations are fully mixed, the coating room particle concentrations can be described with a mass balance of aerosol particles in a single compartment (Hewett and Ganser, 2017):

$$\frac{dN(t)}{dt} = \lambda N_{BG}(t) + \varepsilon_C \frac{S_N(t)}{V} - (\lambda + \lambda_d)N(t) \tag{1}$$

where N (cm^{-3}) is the room particle concentration, $\lambda = \lambda_n + \lambda_C + \lambda_R$ (min^{-1}) is the room total ventilation rate consisting of the natural air exchange λ_n, the LEV$_C$ λ_C, and the LEV$_R$ λ_R, N_{BG} (cm^{-3}) is the background particle concentration coming from outdoors and surrounding compartments, ε_C (−) is the protection factor of the chamber consisting of capturing efficiency of the LEV$_C$ and chamber shielding enclosing the source, S_N (min^{-1}) is the particle emission rate of the source, V (m^3) is the volume of the room, λ_d (min^{-1}) is the particle deposition rate onto surfaces, and t is the time. This can be expressed as:

$$\frac{dN(t)}{dt} = \frac{1}{V}(\overset{=S_{tot}(t)}{\overbrace{QN_{BG}(t) + \varepsilon_C S_N(t)}}) - (\overset{=\gamma}{\overbrace{\lambda + \lambda_d}})N(t) = \frac{1}{V}S_{tot}(t) - \gamma N(t) \tag{2}$$

where S_{tot} (min^{-1}) is the total particle generation rate to the coating room, and γ (min^{-1}) is the total particle decay rate. When the particle emissions from ventilation and indoor sources are negligible (i.e. $S_{tot}(t) \approx 0$ min^{-1}) the coating room particle number concentration decay as follows:

$$N(t) = N_{t=0} \cdot e^{-\gamma \cdot t} \tag{3}$$

According to a convolution theorem, the coating room particle number concentration is a convolution of the particle sources and particle losses as follows (see e.g. Schripp et al., 2008):

$$S_{tot}(t) \cdot N(t) = V \int_0^t (QN_{BG}(t) + \varepsilon_C S_N(t)) \cdot N(t-\tau)d\tau \tag{4}$$

where the particle emission term can be solved with a numerical deconvolution as

$$S_{tot}(t) = V \frac{N(t) - N(t-\Delta t) \cdot e^{-\gamma \cdot \Delta t}}{\Delta t} \tag{5}$$

Particle emission rates were calculated for a pre-activity period when $S_N(t) = 0$ min^{-1} to estimate background particle generation rate $S_{BG}(t) = QN_{BG}(t)$. Because the process chamber protection factor ε_C was not known, we calculated directly the combined $\varepsilon_C S_N$ term instead of the individual values by subtracting S_{BG} from the total particle generation rate during processes.

3. Results and discussion

3.1. Particle concentrations

The results of the particle number concentration measurements were analyzed considering three phases: pre-activity (14:30–15:00), dip coating (15:00–15:10), and a continuous process consisting of two complete process cycles including air blade drying (15:48–16:23; Fig. 2). The process specific average concentrations and emission rates measured in the NF, FF, and BZ are shown in Table 1. Also, concentrations in the NF were measured overnight from end of process to 7:00 next morning by CPC and NanoScan. Concentrations measured between 1:00 and 4:00 are shown in Fig. A.2, Supplementary material. Particle size distributions measured during different phases in the NF are shown in Fig. A.3, Supplementary material. Instrument comparisons were made using pre-activity concentrations, showing that the N_{NF} particle number concentrations measured by NanoScan+OPS were 1.4 to 3.5 times lower than the concentrations measured by other instruments (Fig. 2). Depending on the particle size distribution, concentration, and particle morphology, the deviation in particle number concentration measured by the CPC and NanoScan or DiSCmini can be up to 50% (Fonseca et al., 2016; Ham et al., 2016; Asbach et al., 2017; Todea et al., 2017).

Dip coating did not increase the concentrations from the pre-activity level (Table 1). Air blade cleaning increased concentrations of <200 nm and >400 nm size particles (Fig. 2 and Fig. A.3, Supplementary material). The N_{FF} concentration level followed the N_{NF} and N_{BZ} concentration levels. This indicates that particles were mixed well at all times in the

coating room (Fig. 2). The laboratory room concentrations followed the N_{NF} and N_{FF} concentrations indicating that the air was mixed with laboratory air as well. Concentrations measured from an opening to a hall adjacent to the coating room were not affected notably by the process emissions suggesting that the air flow (N/A m^3 min^{-1}) was from the hall to the coating room.

The continuous process particle number size distributions were averaged over the second $PM_{4,BZ}$ sampling period, which was used to calculate the average particle mass size distribution. Only an upper limit could be assessed for the particle density, because the $PM_{4,BZ}$ concentration was below the detection limit. The respirable mass size distribution, m_{PM4}, corresponds to the $PM_{4,BZ}$ concentration detection limit of 116 µg m^{-3} with a density of 2.2 g cm^{-3}, which corresponds to $m_{<10µm}$ ≤257 µg m^{-3} (Fig. 3).

During night, the average NF particle concentrations in the coating room was 16.5×10^3 cm^{-3} with a particle geometric mean diameter (D_{pg}) of 50 nm and a geometric standard deviation (GSD) of 1.8 (Fig. A.3, Supplementary material). These particles were most likely emitted by a process performed in the adjacent hall, which were then transported to the coating room *via* incoming ventilation air. In industrial settings, high ultrafine particle concentration levels are common and the particles are dispersed easily between different production areas (Viitanen et al., 2017).

3.2. Particle losses and emission rates

During night, the concentration level decreased exponentially from *ca.* 10^4 to 10^3 cm^{-3} between 2:00 and 2:56 (Fig. A.2, Supplementary material). For such concentrations, the coagulation may be considered insignificant, because the particle concentration was <10^4 cm^{-3} and the majority of the particles were between 30 and 200 nm in diameter (Fig. 2b; Yu et al., 2013). This period was used to estimate the decay rates of 1.69 and 1.85 h^{-1} for particles measured by NanoScan and CPC, respectively by using Eq. (3) (Fig. A.2a, Supplementary material). In the numerical deconvolution (Eq. (5)) an average decay rate of 1.77 h^{-1} was used. These decay rates include contributions from particles entering with incoming ventilation air. This does not cause an error, if the incoming air concentration is constant over the coating process measurement period.

During the continuous process, the particle number emission rate in the NF was up to 420×10^9 min^{-1} and LDSA emission rates in BZ was
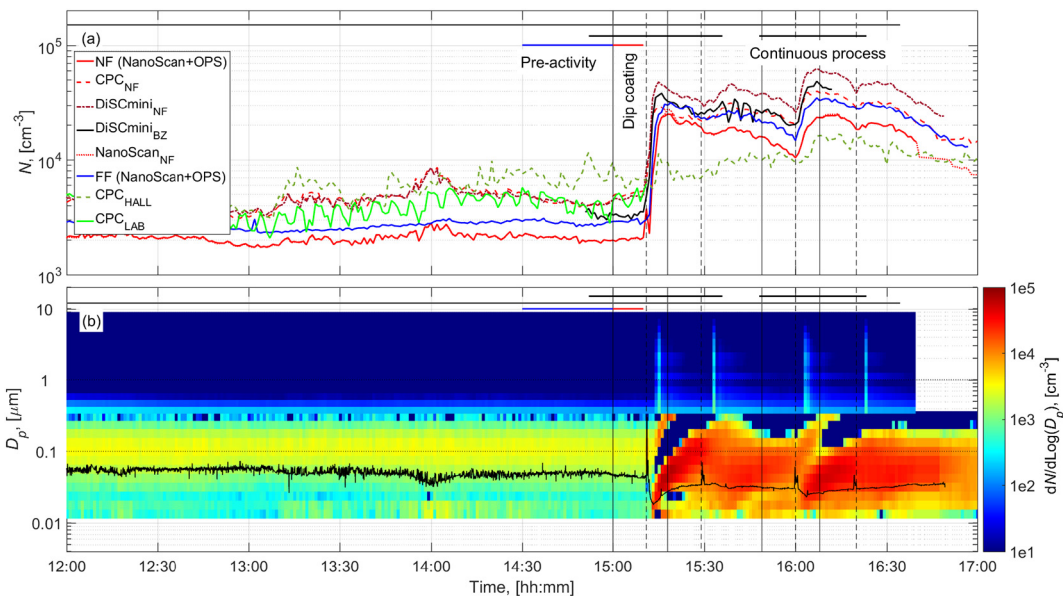

Fig. 2. Concentration time series during the coating: a) particle number concentrations measured from the NF, FF, and BZ, b) particle number size distributions measured from the NF by NanoScan and OPS. The vertical solid and dashed black lines show the start and end times of the dip coating. Air blade drying follows within 1 min after end of the dip coating.

Table 1
Particle concentrations and emission rates in the NF, FF, and BZ.

Process (time)	N_{NF}, ×10³ [cm⁻³]	$S_{N,NF}$, ×10⁹ [min⁻¹]	N_{FF}, ×10³ [cm⁻³]	$S_{N,FF}$, ×10⁹ [min⁻¹]	$LDSA_{BZ}$, [μm² cm⁻³]	$S_{LDSA,BZ}$, ×10⁹ [μm² min⁻¹]	$PM_{4,BZ}$, [μg m⁻³]
Pre-activity (14:30–15:00)	2.1 (1.05)	37 (2.7)	2.8 (1.04)	47 (1.8)	52.8 (1.10)	0.23 (1.9)	95.8[b]
Dip coating (15:00–15:10)	2.0 (1.02)	62 (2.3)	2.9 (1.03)	88 (1.3)	45.4 (1.34)	0.48 (4.6)	95.8[b]
Continuous process (15:48–16:23)	17.5 (1.32)	420 (3.2)	25.1 (1.31)	660 (2.3)	N/A[a]	N/A[a]	<116[c]

[a] Sample from 15:48 to 16:12 (see Fig. 2a).
[b] Sample consist of 7 min 54 s from background and 36 min from process concentrations (see Fig. 2a).
[c] TiO₂ concentration was 4.2 μg m⁻³ according to the SEM/EDS analysis.

1.33×10^9 μm² min⁻¹, respectively (Table 1). The FF emission rates were 1.4 ± 0.2 times higher as expected due to the systematic difference between N_{NF} and N_{FF} particle concentrations. Fig. A.4, Supplementary material, shows the time series of the NF particle number emission rates and the particle number emission rate size distributions. Fig. A.5, Supplementary material, shows the average number emission rate size distributions in NF for pre-activity, dip coating, and continuous process.

Fig. 3 shows the particle mass emission rate distribution calculated from the average particle number emission rate size distribution in NF measured during the continuous process using a particle density of 2.2 g cm⁻³. Furthermore, from the mass emission rate distribution was calculated the respirable mass emission rate distribution according to Hinds (1999). The average particle number- and mass emission rate distributions for the continuous process are given in the Appendix D, Supplementary material.

3.3. Composition of the particles

TEM analyses show that TiO₂ was present in two forms, which were named here as fine TiO₂ (fTiO₂) with a primary particle size >40 nm (primary particle size distribution not shown) and as nTiO₂ with a primary particle size of ~5 nm (Fig. 4). Airborne nTiO2 particles had similar size and structure as the ones sampled from the photoactive suspension (Fig. A.1, Supplementary material). The relative abundances of fTiO₂ and nTiO₂ particles are not known. The fTiO2 particles were not found in the photoactive suspension. The fTiO₂ and nTiO₂ were both present in individual particles as well as agglomerates of up to several micrometers in diameter (Figs. 4 and 5). Other particles collected on the TEM samples were soot, salt condensates and condensed organic matter on which nTiO₂ particles were deposited. Fig. 5c shows an example where nTiO₂ primary single particles were deposited onto a soot particle surface.

SEM/EDS analyses are summarized in Fig. 6, displaying the relative number abundance of those particles containing no Ti (red), or approximately up to a third (green), two thirds (blue) or more than two thirds (turquoise) of Ti in their mass in the size intervals <0.25 μm, 0.25 to 1 μm, and >1 μm. The plots show that the 30% and 57% of particles collected inside the fume hood and in the worker breathing zone contained Ti, respectively. The fraction of particles containing Ti was higher towards larger particles and in total there was more Ti in the breathing zone than in the fume hood (Fig. 6). We interpret the findings so that fTiO₂ and nTiO₂ are released as individual primary particles during the air blade drying process and dispersed during transport to the breathing zone, where they mix internally and/or settle on to other, larger particles.

XRF-analysis showed that the FF and the continuous process BZ PM₄ filter samples contained 0.76 and 0.78 μg TiO₂, respectively (see the sampling periods from Fig. 2). Because the particles were well mixed in the coating room air, the TiO₂ particles on the FF PM₄ sample most likely originated from the process. The respirable mass concentration of TiO₂ during the continuous process measured from the workers breathing zone was 4.2 μg m⁻³.

3.4. Risk assessment

Our analysis showed that the average personal respirable mass concentration was <116 μg m⁻³ during the 35 min completion of two coating and drying cycles. Electron microscopy analysis showed that the personal respirable dust exposure consisted of primarily TiO₂, soot, organic matter, and various salts while WDXRF showed an average concentration of only 4.2 μg m⁻³ TiO₂.

NIOSH (2011) recommend an 8-hour occupational exposure limit for respirable nTiO₂ of 300 μg m⁻³ and recently Thompson et al. (2016) assessed that at a daily respirable TiO₂ concentration of

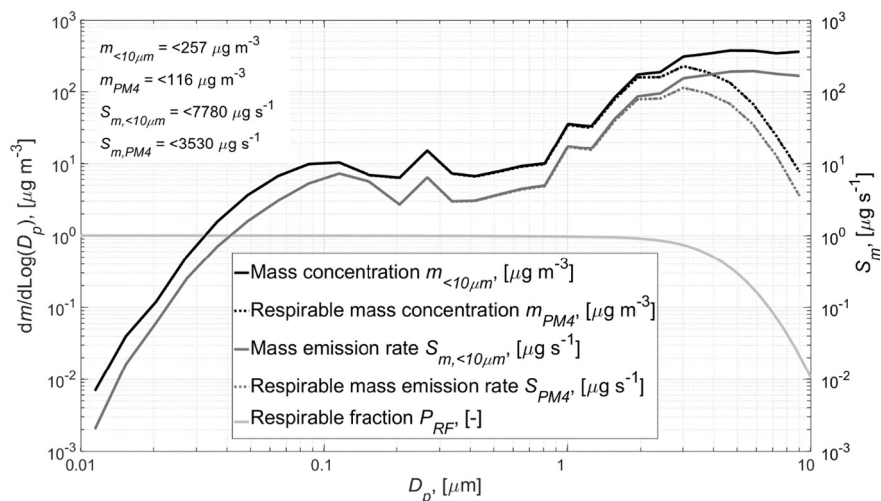**Fig. 3.** Average mass concentrations and emission rates for concentrations measured between 10 nm and 10 μm and weighted with respirable fraction P_{RF} during the continuous process measured between 15:48–16:23.
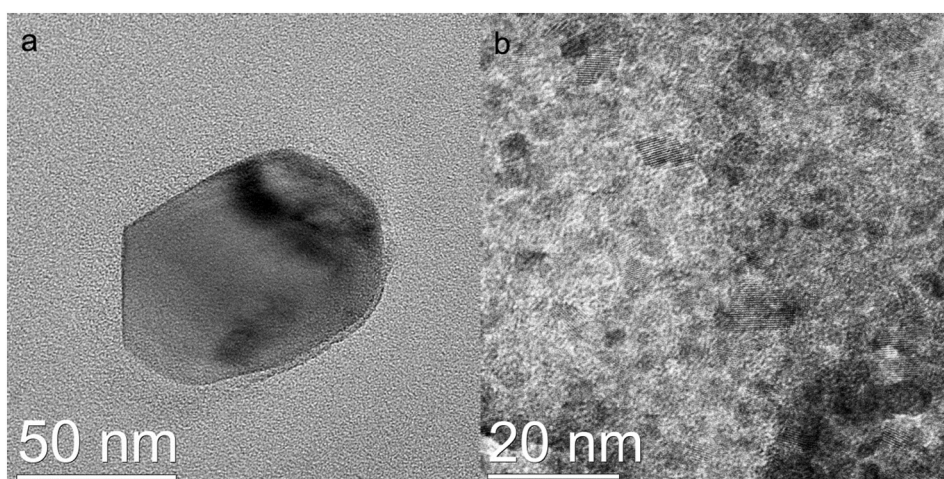
Fig. 4. Two forms of TiO₂ sampled inside the fume hood: a) TiO₂ and b) nTiO₂ with primary particle size of 5 nm.

3.6 μg m^{-3} bronchioalveolar tumors would be induced at a frequency of 10^{-5} per year.

Thompson et al. (2016) derived a daily no significant risk dose level (NSRL) for the nonlinear mode of action involving particle overload, chronic inflammation and cell proliferation (NSRLa) and a low-dose linear extrapolation for tumor incidence (NSRLb). The limit values for NSRLa was 300 μg day^{-1} and 44 μg day^{-1} for NSRLb. During the continuous process the mass concentration of $D_p < 10$ μm particles ($m_{<10\mu m}$) was <257 μg m^{-3} (Appendix D, Supporting information) which resulted in an overall inhalation dose rate of <5.6 μg min^{-1}. The particles were deposited mainly in the upper airways (87%) while the depositions in the trachea-bronchial and alveolar regions was 5 and 8%, respectively. During the continuous process, an 8-hour exposure without use of respirator would result in deposition of a total mass of <2.7 mg and 98 μg of TiO₂ assuming that Ti is distributed uniformly across the mass size distribution. Assuming that only particles deposited to the trachea-bronchial and alveolar regions are causing the potential health effects, the biologically relevant TiO₂ dose would be 13 μg, which is clearly below the NSRL values derived by Thompson et al. (2016). Here,

including a bronchial dose as biologically active is precautionary because of the high trachea-bronchial clearance (Thomas, 2013).

Recently, Schmid and Stoeger (2016) assessed the relation between particles' dry powder Brunner-Emmett-Teller (BET) surface area dose in cm² g^{-1} and polymorphonuclear neutrophil (PMN) influx. The experiments were performed by single intratracheal instillation of granular biodurable particles, such as TiO₂, in the lungs of rats and mice. This relation was used by Koivisto et al. (2016) to estimate workers' risk for suffering acute pulmonary inflammation by comparing the human equivalent LDSA 8-h with the NOEL$_{1/100}$, the one hundredth of the no observed effect level (no inflammation) derived from Schmid and Stoeger (2016). The lung-weight normalized NOEL$_{1/100}$ was 0.11 cm² g^{-1} for granular biodurable particles. Here, the LDSA concentration during the continuous process was 30.3 μm² cm^{-3} corresponding to the human equivalent dose of 4.3×10^{-3} cm² g^{-1} during 8-hour of exposure (see calculation details from Koivisto et al., 2016). Consequently, in the specific scenarios studied, there appears to be a low risk of exceeding the critical threshold concentration for induction of any reported nano-TiO₂-exposure-related disease. The LDSA exposure level was as low
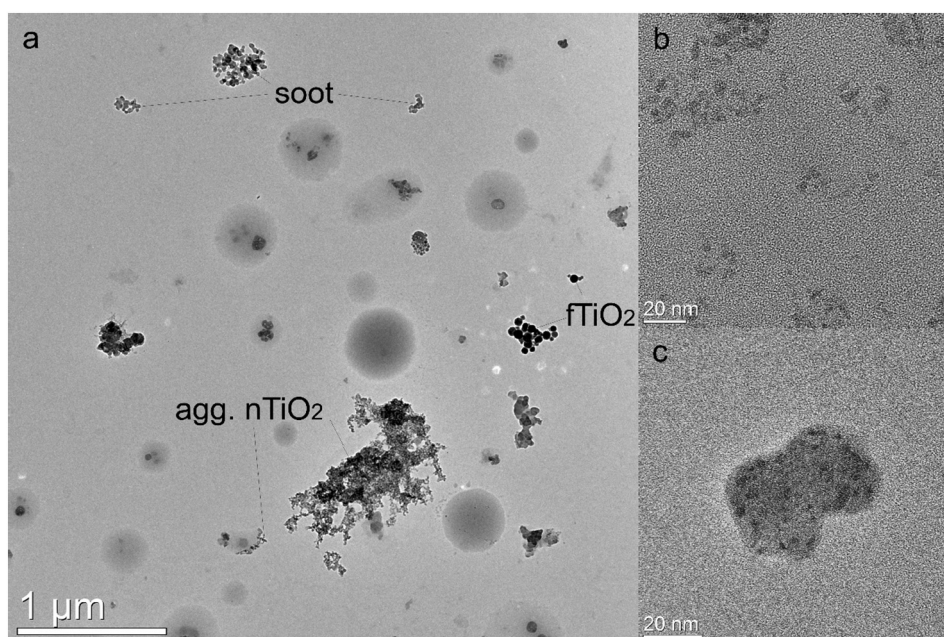

Fig. 5. Particles sampled from the BZ during the continuous process: a) agglomerates of TiO₂, nTiO₂, soot particles, and their mixtures, b) agglomerated and individual nTiO₂ particles, b) nTiO₂ particles onto a soot particle surface.
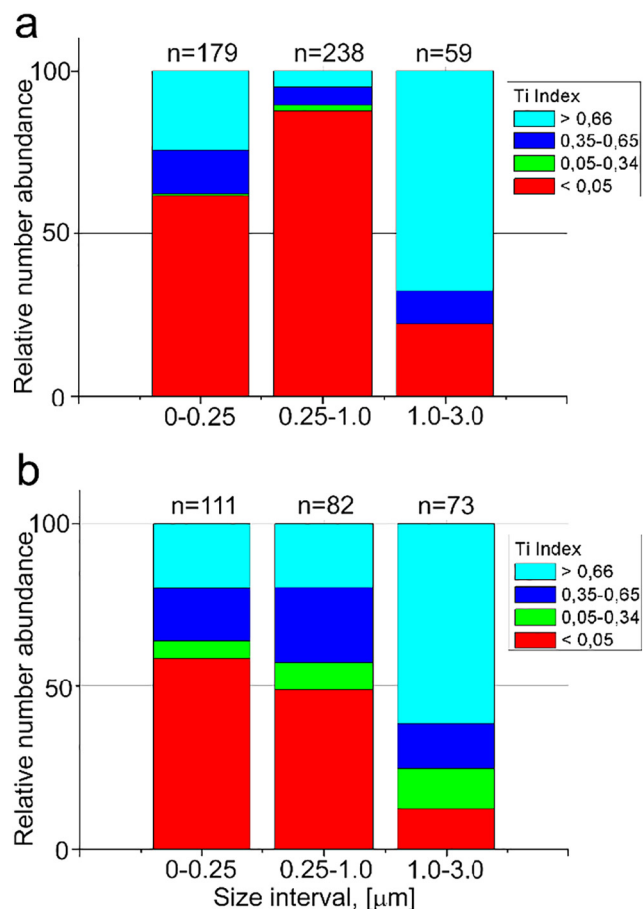
Fig. 6. Ti index, obtained from SEM/EDS analyses, a) in the fume hood and b) in the breathing zone. Number of analyzed particles is shown top of each bar. (For interpretation of the references to color in this figure legend, the reader is referred to the web version of this article.)

compared to particle concentrations in urban background measurements in different cities yielding a geometric mean LDSA concentration level of 44.2 μm^2 cm^{-3} (Koivisto et al., 2016).

3.5. Recommendations for emission control

The dip coating did not release detectable amounts of particles. However, the coating chamber has insufficient emission control for air blade drying. The coating chamber exhaust air streamlines are oppositely directed to the air blade streamlines. This causes air mixing and air release from the partly open chamber. In addition, the exhaust air volume flow must be higher than the air volume (N/A) flow from the air blade. Due to the improper chamber design, the air blade drying increased the particle number concentration levels nine times from the pre-activity level in the coating room and laboratory. Based on the 8-hour exposure during the continuous process and the NSRLs, the workers are recommended to wear respirators during the continuous process both in the coating room and in the adjacent laboratory room if the door is not closed.

3.6. Recommendations for exposure modeling

The emission rates assigned in this study are a product of the process particle generation rate and the protection factor of the coating chamber. The dip coating did not release detectable amounts of airborne particles from the coating chamber to the room. The air blade drying released particles from the chamber to the room at a rate of 420 $\times 10^9$ min^{-1}, 1.33 $\times 10^9$ μm^2 min^{-1}, and 3.5 mg min^{-1} (respirable

fraction). The particles were fully mixed in the 390 m^3 room within less than a minute. Thus, it was concluded that a single compartment model in this case was sufficient for the indoor particle concentration modeling.

4. Conclusions

Here, a photoactive suspension based on nanoscale TiO_2 was applied on ceramic honeycomb cells. For the coating process, we assessed process particle emissions, exposure levels, and dose rates for all particles and TiO_2 particles. The health risk associated with TiO_2 exposure was estimated by using three different methods; 1) by comparing TiO_2 exposure levels with the recommended exposure limits, 2) by comparing inhaled TiO_2 deposited dose during 8-hour exposure with a daily no significant risk dose level, and 3) by comparing human equivalent surface area dose with one-hundredth of the NOEL.

Dip coating of ceramics did not release detectable amounts of particles. An air blade drying process increased the particle concentrations in the coating room to on average 2.5 $\times 10^4$ cm^{-3}, 30.3 μm^2 cm^{-3}, and <116 μg m^{-3} and the particles were well mixed in the room. The $nTiO_2$ was abundant in different particle phases and present in particles at all size ranges. The emission rates calculated using the convolution theorem were 420 $\times 10^9$ min^{-1} (1.33 $\times 10^9$ μm^2 min^{-1} and <3.5 mg min^{-1}). The calculated inhalation dose rate of particles below 10 μm in diameter was <5.6 μg min^{-1} whereof 3.7% consisted of TiO_2. During 8-hour exposure without use of respirators, the total calculated deposited dose would be <2700 μg where 87% of the particles would be deposited in the upper airways. The fraction of TiO_2 deposited to the trachea-bronchial and alveolar regions was 13 μg. If this is considered as the biologically relevant TiO_2 dose, the dose was well below a daily no significant risk dose levels (NRSL) for chronic inflammation and cell proliferation and for tumor incidence of 300 and 44 μg day^{-1}, respectively.

Appendix A. Dip coating of air purifier ceramic honeycombs with photocatalytic TiO_2 nanoparticles: a case study for occupational exposure

Appendix A shows supplementary material for the data analysis. PARNASOS® PH000025 material data sheet is given in Appendix B and the material safety data sheet is given in Appendix C. Numeric values of concentrations and emission rates are given in Appendix D. Supplementary data to this article can be found online at https://doi.org/10.1016/j.scitotenv.2018.02.316.

References

Asbach, C., Alexander, C., Clavaguera, S., Dahmann, D., Dozol, H., Faure, B., Fierz, M., Fontana, L., Iavicoli, I., Kaminski, H., MacCalman, L., Meyer-Plath, A., Simonow, B., van Tongeren, M., Todea, A.M., 2017. Review of measurement techniques and methods for assessing personal exposure to airborne nanomaterials in workplaces. Sci. Total Environ. 15 (603–604), 793–806.

Chen, J., Qiu, F., Xu, Q., Cao, S., Zhu, H., 2015. Recent progress in enhancing photocatalytic efficiency of TiO2-based materials. Appl. Catal. A Gen. 495, 131–140.

Cheng, Y.S., 2001. Condensation detection and diffusion size separation techniques. In: Baron, P.A., Willeke, K. (Eds.), Aerosol Measurements: Principles, Techniques and Applications. Wiley-Interscience, New York, pp. 569–601.

Demou, E., Stark, W.J., Hellweg, S., 2009. Particle emission and exposure during nanoparticle synthesis in research laboratories. Ann. Occup. Hyg. 58, 829–838.

European Environmental Agency, 2017. Air Quality in Europe — 2017 Report. https://doi.org/10.2800/358908.

Fonseca, A.S., Viana, M., Pérez, N., Alastuey, A., Querol, X., Kaminski, H., Todea, A.M., Monz, C., Asbach, C., 2016. Intercomparison of a portable and two stationary mobility particle sizers for nanoscale aerosol measurements. Aerosol Sci. Technol. 50, 653–668.

Fonseca, A.S., Kuijpers, E., Kling, K.I., Levin, M., Koivisto, A.J., Nielsen, S.H., Fransman, W., Fedutik, Y., Jensen, K.A., Koponen, I.K., 2018. Particle release and control of worker exposure during laboratory-scale synthesis, handling and simulated spills of manufactured nanomaterials in fume-hoods. J. Nanopart. Res. https://doi.org/10.1007/s11051-018-4136-3.

Ganser, G.H., Hewett, P., 2017. Models for nearly every occasion: part II - two box models. J. Occup. Environ. Hyg. 14, 58–71.

Garcia-Segura, S., Brillas, E., 2017. Applied photoelectrocatalysis on the degradation of organic pollutants in wastewaters. J Photochem Photobiol C: Photochem Rev 31, 1–35.

Ham, S., Lee, N., Eom, I., Lee, B., Tsai, P.J., Lee, K., Yoon, C., 2016. Comparison of real time nanoparticle monitoring instruments in the workplaces. Saf. Health Work 7, 381–388.

Health Effects Institute, 2017. State of Global Air 2017. Special Report. Health Effects Institute, Boston, MA.

Hewett, P., Ganser, G.H., 2017. Models for nearly every occasion: part I - one box models. J. Occup. Environ. Hyg. 14, 49–57.

Hinds, W.C., 1999. Uniform particle motion. In: Hinds, W.C. (Ed.), Aerosol Technology: Properties, Behavior, and Measurement of Airborne Particles, 2nd ed. John Wiley & Sons Inc., New York, NY, USA, pp. 233–259 (ch. 11).

ICRP, 1994. Human respiratory tract model for radiological protection. Ann. ICRP 24, 1–482.

Kaminski, H., Beyer, M., Fissan, H., Asbach, C., Kuhlbusch, T.A.J., 2015. Measurements of nanoscale TiO_2 and Al_2O_3 in industrial workplace environments – methodology and results. Aerosol Air Qual. Res. 15, 129–141.

Kandler, K., Benker, N., Bundke, U., Cuevas, E., Ebert, M., Knippertz, P., Rodriguez, S., Schütz, L., Weinbruch, S., 2007. Chemical composition and complex refractive index of Saharan Mineral Dust at Izaña, Tenerife (Spain) derived by electron microscopy. Atmos. Environ. 41, 8058–8074.

Kandler, K., Lieke, K., Benker, N., Emmel, C., Küpper, M., Müller-Ebert, D., Ebert, M., Scheuvens, D., Schladitz, A., Schütz, L., Weinbruch, S., 2011. Electron microscopy of particles collected at Praia, Cape Verde, during the Saharan Mineral Dust Experiment: particle chemistry, shape, mixing state and complex refractive index. Tellus B 63, 475–496.

Kling, K.I., Levin, M., Jensen, A.C.Ø.K., Jensen, A., Koponen, I.K., 2016. Size-resolved characterization of particles and fibers released during abrasion of fiber-reinforced composite in a workplace influenced by ambient background sources. Aerosol Air Qual. Res. 16, 11–24.

Koivisto, A.J., Aromaa, M., Mäkelä, J.M., Pasanen, P., Hussein, T., Hämeri, K., 2012a. Concept to estimate regional inhalation dose of industrially synthesized nanoparticles. ACS Nano 6, 1195–1203.

Koivisto, A.J., Lyyränen, J., Auvinen, A., Vanhala, E., Hämeri, K., Tuomi, T., Jokiniemi, J., 2012b. Industrial worker exposure to airborne particles during the packing of pigment and nanoscale titanium dioxide. Inhal. Toxicol. 24, 839–849.

Koivisto, A.J., Aromaa, M., Koponen, I.K., Fransman, W., Jensen, K.A., Mäkelä, J.M., Hämeri, K.J., 2015. Workplace performance of a loose-fitting powered air purifying respirator during nanoparticle synthesis. J. Nanopart. Res. 17, 177.

Koivisto, A.J., Kling, K.I., Levin, M., Fransman, W., Gosens, I., Cassee, F.R., Jensen, K.A., 2016. First order risk assessment for nanoparticle inhalation exposure during injection molding of polypropylene composites and production of tungsten-carbide-cobalt fine powder based upon pulmonary inflammation and surface area dose. Nano 6, 30–38.

Koivisto, A.J., Jensen, A.C.Ø., Kling, K.I., Nørgaard, A., Brinch, A., Christensen, F., Jensen, K.A., 2017. Quantitative material releases from products and articles containing manufactured nanomaterials: towards a release library. Nano 5, 119–132.

Koivisto, A.J., Jensen, A.C.Ø., Kling, K.I., Kling, J., Budtz, H.C., Koponen, I.K., Tuinman, I., Hussein, T., Jensen, K.A., Nørgaard, A., Levin, M., 2018. Particle emission rates during electrostatic spray deposition of TiO_2 nanoparticle-based photoactive coating. J. Hazard. Mater. 341, 218–227.

Lee, J.H., Kwon, M., Ji, J.H., Kang, C.S., Ahn, K.H., Han, J.H., Yu, I.J., 2011. Exposure assessment of workplaces manufacturing nanosized TiO2 and silver. Inhal. Toxicol. 23, 226–236.

Lieke, K., Kandler, K., Scheuvens, D., Emmel, C., Von Glahn, C., Petzold, A., Weinzierl, B., Veira, A., Ebert, M., Weinbruch, S., Schütz, L., 2011. Particle chemical properties in the vertical column based on aircraft observations in the vicinity of Cape Verde Islands. Tellus B 63, 497–511.

Lieke, K.I., Rosenørn, T., Pedersen, J., Larsson, D., Kling, J., Fuglsang, K., Bilde, M., 2013. Micro- and nanostructural characteristics of particles before and after an exhaust gas recirculation system scrubber. Aerosol Sci. Technol. 47, 1038–1046.

Mamaghani, A.H., Haghighat, F., Lee, C.-S., 2017. Photocatalytic oxidation technology for indoor environment air purification: the state-of-the-art. Appl. Catal. B Environ. 203, 247–269.

Mihalache, R., Verbeek, J., Graczyk, H., Murashov, V., van Broekhuizen, B., 2017. Occupational exposure limits for manufactured nanomaterials, a systematic review. Nanotoxicology 2017 (11), 7–19.

Mo, J., Zhang, Y., Xu, Q., Lamson, J.J., Zhao, R., 2009. Photocatalytic purification of volatile organic compounds in indoor air: a literature review. Atmos. Environ. 43, 2229–2246.

NIOSH, National Institute for Occupational Safety and Health, 2011. NIOSH Current Intelligence Bulletin 63: Occupational Exposure to Titanium Dioxide. Department of Health and Human Services. Public Health Service. Centers for Disease Control and Prevention. NIOSH Publication No. 2011–160.

Ortelli, S., Poland, C.A., Baldi, G., Costa, A.L., 2016. Silica matrix encapsulation as a strategy to control ROS production while preserving photoreactivity in nano-TiO_2. Environ. Sci. Nano 3, 602–610.

Piccinno, F., Gottschalk, F., Seeger, S., Nowack, B., 2012. Industrial production quantities and uses of ten engineered nanomaterials in Europe and the world. J. Nanopart. Res. 14, 1109.

Puddu, V., Choi, H., Dionysiou, D.D., Puma, G.L., 2010. TiO_2 photocatalyst for indoor air remediation: influence of crystallinity, crystal phase, and UV radiation intensity on trichloroethylene degradation. Appl. Catal. B Environ. 94, 211–218.

Ramos-Delgado, N.A., Gracia-Pinillaa, M.Á., Mangalaraja, R.V., O'Shea, K., Dionysiou, D.D., 2016. Industrial synthesis and characterization of nanophotocatalysts materials: titania. Nanotechnol. Rev. 5, 467–479.

Ren, H., Koshy, P., Chen, W.-F., Qi, S., Sorrell, C.C., 2017. Photocatalytic materials and technologies for air purification. J. Hazard. Mater. 325, 340–366.

Rissler, J., Nordin, E.Z., Eriksson, A.C., Nilsson, P.T., Frosch, M., Sporre, M.K., Wierzbicka, A., Svenningsson, B., Löndahl, J., Messing, M.E., Sjogren, S., Hemmingsen, J.G., Loft, S., Pagels, J.H., Swietlicki, E., 2014. Effective density and mixing state of aerosol particles in a near-traffic urban environment. Environ. Sci. Technol. 48, 6300–6308.

Robichaud, C.O., Uyar, A.E., Darby, M.R., Zucker, L.G., Wiesner, M.R., 2009. Estimates of upper bounds and trends in nano-TiO_2 production as a basis for exposure assessment. Environ. Sci. Technol. 43, 4227–4233.

Rostedt, A., Marjamäki, M., Keskinen, J., 2009. Modification of the ELPI to measure mean particle effective density in real-time. J. Aerosol Sci. 40, 823–831.

Schmid, O., Stoeger, T., 2016. Surface area is the biologically most effective dose metric for acute nanoparticle toxicity in the lung. J. Aerosol Sci. 99, 133–143.

Schripp, T., Wensing, M., Uhde, E., Salthammer, T., He, C., Morawska, L., 2008. Evaluation of ultrafine particle emissions from laser printers using emission test chambers. Environ. Sci. Technol. 42, 4338–4343.

Spinazzè, A., Cattaneo, A., Limonta, M., Bollati, V., Bertazzi, P.A., Cavallo, D.M., 2016. Titanium dioxide nanoparticles: occupational exposure assessment in the photocatalytic paving production. J. Nanopart. Res. 18, 151.

Szczepanik, B., 2017. Photocatalytic degradation of organic contaminants over clay-TiO_2 nanocomposites: a review. Appl. Clay Sci. 141, 227–239.

Thomas, R.J., 2013. Particle size and pathogenicity in the respiratory tract. Virulence 4, 847–858.

Thompson, C.M., Suh, M., Mittal, L., Wikoff, D.S., Welsh, B., Proctor, D.M., 2016. Development of linear and threshold no significant risk levels for inhalation exposure to titanium dioxide using systematic review and mode of action considerations. Regul. Toxicol. Pharmacol. 80, 60–70.

Todea, A.M., Beckmann, S., Kaminski, H., Bard, D., Bau, S., Clavaguera, S., Dahmann, D., Dozol, H., Dziurowitz, N., Elihn, K., Fierz, M., Lidén, G., Meyer-Plath, A., Monz, C., Neumann, V., Pelzer, J., Simonow, B.K., Thali, P., Tuinman, I., van der Vleuten, A., Vroomen, H., Asbach, C., 2017. Inter-comparison of personal monitors for nanoparticles exposure at workplaces and in the environment. Sci. Total Environ. 15 (605–606), 929–945.

Viitanen, A.-K., Uuksulainen, S., Koivisto, A.J., Hämeri, K., Kauppinen, T., 2017. Workplace measurements of ultrafine particles—a literature review. Ann. Work Expo. Health 61, 749–758.

Vratolis, S., Fetfatzis, P., Argyrouli, A., Papayannis, A., Müller, D., Veselovskii, I., Bougiatioti, A., Nenes, A., Remoundaki, E., Diapouli, E., Manousakas, M., Mylonaki, M., Eleftheriadis, K., 2018. A new method to retrieve the real part of the equivalent refractive index of atmospheric aerosols. J. Aerosol Sci. 117, 54–62.

Xu, H., Zhao, L., Chen, Z., Zhou, J., Tang, S., Kong, F., Li, X., Yan, L., Zhang, J., Jia, G., 2016. Exposure assessment of workplace manufacturing titanium dioxide particles. J. Nanopart. Res. 18, 288.

Yu, C.W.F., Kim, J.T., 2013. Photocatalytic oxidation for maintenance of indoor environmental quality. Indoor Built Environ. 22, 39–51.

Yu, M., Koivisto, A.J., Hämeri, K., Seipenbusch, M., 2013. Size dependence of the ratio of aerosol coagulation to deposition rates for indoor aerosols. Aerosol Sci. Technol. 47, 427–434.

Zhong, L., Haghighat, F., 2015. Photocatalytic air cleaners and materials technologies - abilities and limitations. Build. Environ. 91, 191–203.